$(NH_4)(BH_3NH_2BH_2NH_2BH_3)$

$NH_3BH_3NH_2BH_2NH_2BH_3 +H_2$

Family of N & B-based hydrogen stores has now been enlarged by a novel dachshund-like ionic derivative, $NH_4(BH_3NH_2BH_2NH_2BH_3)$, which forms cocrystals with related, partly dehydrogenated, molecular $NH_3BH_2NH_2BH_2NH_2BH_3$. These enormously hydrogen-rich systems easily release hydrogen gas upon thermal activation.

Towards hydrogen-rich ionic $(NH_4)(BH_3NH_2BH_2NH_2BH_3)$ and related molecular $NH_3BH_2NH_2BH_2NH_2BH_3$

ROYAL SOCIETY
OF **CHEMISTRY**

rsc.li/dalton

## PAPER

Check for updates

# Towards hydrogen-rich ionic (NH₄)(BH₃NH₂BH₂NH₂BH₃) and related molecular NH₃BH₂NH₂BH₂NH₂BH₃†‡

Rafał Owarzany, [ID] *[a] Tomasz Jaroń, [ID] [b] Krzysztof Kazimierczuk, [ID] [a] Przemysław J. Malinowski, [ID] [a] Wojciech Grochala [ID] [a] and Karol J. Fijalkowski [ID] *[a]

Attempts of the synthesis of ionic (NH₄)(BH₃NH₂BH₂NH₂BH₃) *via* a metathetical approach resulted in a mixture of the target compound and partly dehydrogenated molecular NH₃BH₂NH₂BH₂NH₂BH₃ product. The mixed specimen was characterised by NMR and vibrational spectroscopies, and the cocrystal structure was analyzed from powder X-ray diffraction data supported by theoretical density functional theory calculations. The compound crystallises in a $P2_1/c$ unit cell with the lattice parameters of $a$ = 13.401(11) Å, $b$ = 13.196(8) Å, $c$ = 17.828(12) Å, $\beta$ = 128.83(4)°, $V$ = 2556(3) Å³ and $Z$ = 16. Despite their impressive hydrogen content, similar to ammonia borane, both title compounds release hydrogen substantially polluted with borazine and traces of ammonia and diborane.

## Introduction

Protic-hydridic compounds constitute an important family of solid-state hydrogen storage materials with the potential to be applied as onboard fuel systems required in hydrogen economy. The presence of both positively and negatively charged hydrogen atoms results in the formation of a network of dihydrogen bonds governing the crystal structure and facilitating the process of thermal decomposition.[1] These features were observed and thoroughly described for ammonia borane[2] and metal amidoboranes[3] and further explored for NH₄BH₄.[4]

Ammonia borane is one of the best-researched materials in this group, being an air- and water-insensitive solid containing *ca.* 19.6% of hydrogen by weight.[5,6] Unfortunately, ammonia borane releases only 1/3 of the stored hydrogen below 120 °C.[7,8] Moreover, the hydrogen released is contaminated with ammonia, diborane, borazine, aminoborane and aminodiborane, which excludes its use as a direct H₂ source for low-temperature fuel cells.[9] Such high gravimetric H content, however, provides significant room for modifications; even if relatively heavy elements are introduced, the system still

should be able to fulfil gravimetric DOE requirements for hydrogen storage materials (Fig. 1).[10]

Among the derivatives of ammonia borane, amidoborane salts of general formula M(NH₂BH₃)ₙ [abbreviated here as MAB or M(AB)ₙ] constitute the largest group.[11,12] Two dozens of mono- and bimetallic amidoborane salts have been reported. Some of them [*i.e.* KAB,[13] RbAB,[14,15] CsAB,[14,15] Mg(AB)₂,[16] Ba(AB)₂,[17] Al(AB)₃,[18] LiAl(AB)₄,[19] Li₂Mg(AB)₄[20]] evolve pure H₂ upon thermal decomposition at *ca.* 100 °C. Nonetheless, all these materials suffer from a lack of reversibil-



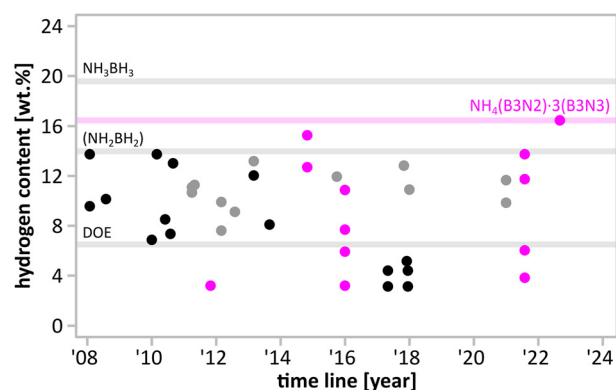**Fig. 1** Hydrogen content of monometallic amidoboranes (black), bimetallic amidoboranes (grey), and M(B3N2) salts (magenta) as a function of reporting date. Hydrogen content of NH₃BH₃ (19.6%) polymeric (NH₂BH₂) (14.0%) and DOE ultimate target (6.5%) are given as a reference. A detailed figure with references to each point is given in ESI (Fig. S1.1†).

*ᵃCentre of New Technologies, University of Warsaw, ul. Banacha 2c, 02-097 Warsaw, Poland. E-mail: r.owarzany@cent.uw.edu.pl, karol.fijalkowski@cent.uw.edu.pl*
*ᵇFaculty of Chemistry, University of Warsaw, ul. Pasteura 1, 02-089 Warsaw, Poland*
†This work is dedicated to Prof. Roald Hoffmann at his 85th birthday
‡Electronic supplementary information (ESI) available: Synthesis, NMR, IR, Raman, PXD, crystal structures, TGA/DSC/MS, DFT results and comparison with other M(B3N2) salts. Detailed data for the main product and reference data for M(BH₃NH₂BH₂NH₂BH₃) salts. See DOI: https://doi.org/10.1039/d2dt03674f
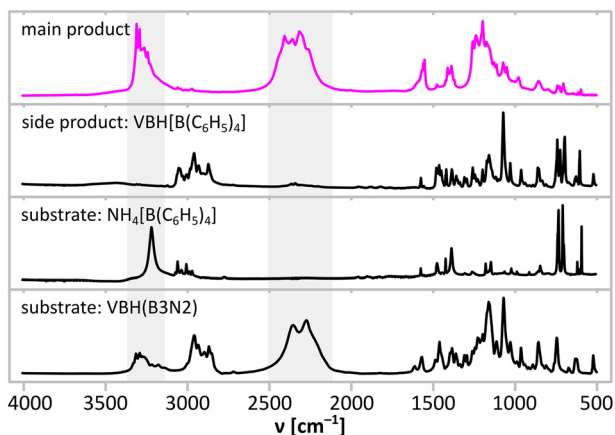
**Fig. 2** Comparison of IR absorption spectra of precursors and products of metathetical synthesis performed according to eqn (1). NH stretching and BH stretching regions are marked with grey fields.
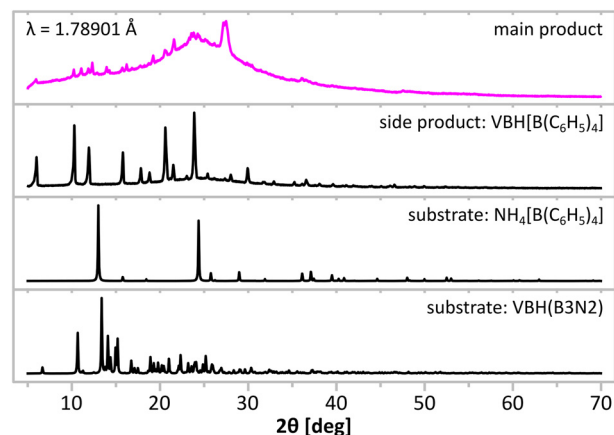


**Fig. 3** Comparison of powder X-ray diffraction patterns of precursors and products of metathetical synthesis performed according to eqn (1). $CoK_{\alpha1,2}$, $\lambda$ = 1.78901 Å.
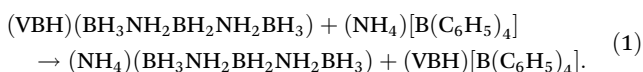
ity and relatively low hydrogen content available at moderate temperatures.[11,12]

Recently, a novel group of ammonia borane derivatives containing five-membered chain anions of general formula $M(BH_3NH_2BH_2NH_2BH_3)$ [abbreviated here as M(B3N2)] have been reported.[21–25] Among them, one can list two allotropes of Verkade's base salt,[22,23] five alkali metal salts[21,23,24,26,27] and four ionic liquids.[25] Although three of them [*i.e.* Li(B3N2),[23,24] $(Bu_4N)(B3N2)$[25] and $(Et_4N)(B3N2)$[25]] meet the target H wt% content and release pure hydrogen below 150 °C, none of them fulfils all the DOE targets simultaneously.[10]

## Results and discussion

### Synthesis

Synthesis of $(NH_4)(B3N2)$ was attempted employing Jaroń *et al.*'s metathetical approach mediated by precursors containing weakly coordinating ions.[28–30] The reaction was conducted in dry THF similarly to the previous syntheses of all alkali metal M(B3N2) salts[23] according to eqn (1):

$$(VBH)(BH_3NH_2BH_2NH_2BH_3) + (NH_4)[B(C_6H_5)_4]$$
$$\rightarrow (NH_4)(BH_3NH_2BH_2NH_2BH_3) + (VBH)[B(C_6H_5)_4]. \quad (1)$$

Unexpectedly, during the reaction, we observed the evolution of a small amount of gas, which should not occur in a metathetical reaction. Since the expected main product contains ammonium cation and B3N2⁻ anion (essentially, a derivative of a borohydride anion), we assumed that – similarly to what is observed for $NH_4BH_4$[31] – hydrogen might be evolved upon reaction of these ions according to eqn (2):

$$(NH_4)(BH_3NH_2BH_2NH_2BH_3) \rightarrow NH_3BH_2NH_2BH_2NH_2BH_3 + H_2 \uparrow. \quad (2)$$
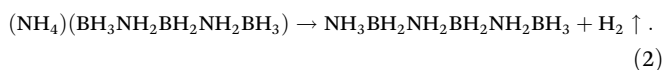
Confirmation that this surmise is correct is presented below.

Synthesis led to a mixture of well-THF-soluble products, which were separated by precipitation of the side product

$(VBH)[B(C_6H_5)_4]$ in dry DCM. Both products were subjected to spectroscopic analyses (Fig. 2) and powder X-ray diffraction (Fig. 3) to demonstrate successful ion exchange according to eqn (1). Indeed, IR spectra (Fig. 2) of the products show that the target product contains NH and BH groups, while the side product contains CH groups. Unfortunately, complete separation of the main and side products was not achieved, as documented by very weak CH bands at *ca.* 3000 cm⁻¹ from $B(C_6H_5)_4^-$ anions for the former, and very weak BH bands at *ca.* 2400 cm⁻¹ from (B3N2)⁻ anions for the latter product. X-ray diffraction points to the same conclusion, showing that two new distinct crystalline species formed during the reaction (Fig. 3). The diffraction patterns of the products are free from reflections coming from the substrates, which suggests at least 95% purity of the former, considering the crystalline phases. However, as the PXRD pattern of the main product contains significant contribution from the amorphous phase (seen as broad humps), such analysis must be treated with care and backed up with the spectroscopic data discussed below.

### NMR spectra

A detailed ¹¹B NMR investigation of the main product dissolved in THF-$d_8$ was performed (Fig. 4). A typical spectrum of M(B3N2) salt consists of a triplet at *ca.* −8.5 ppm from $[BH_2]$ groups and a quartet at *ca.* −22.5 ppm from $[BH3]$ groups, having a relative intensity of 1 : 2.[20,21] Here, the spectrum of the main product is more complicated and contains two triplets ($\delta$ = −10.4 ppm, $J$ = 101 Hz; $\delta$ = −12.3 ppm, and $J$ = 102 Hz) and a quartet ($\delta$ = −22.2 ppm and $J$ = 91 Hz) in an intensity ratio that varies from batch to batch (in average *ca.* 4 : 3 : 5). These features altogether suggest that the main product formed according to (eqn (1)) partially undergoes a subsequent dehydrogenation reaction (eqn (2)). Variation in the observed intensity ratio of the signals may be caused by the partial decomposition of the main product, thus changing the ratio between the components of the product. We note that a 1 : 3 mixture of $(NH_4)(B3N2)$ and $NH_3BH_2NH_2BH_2NH_2BH_3$
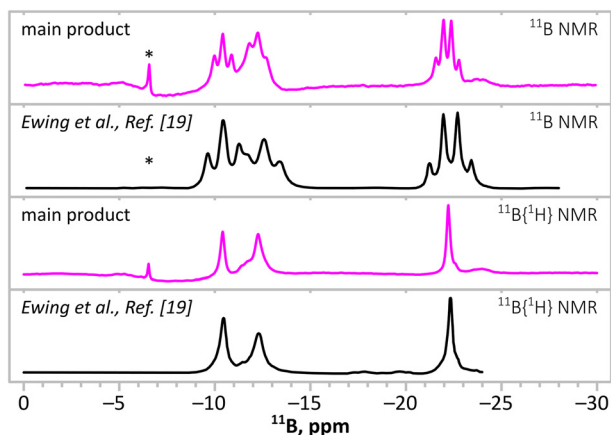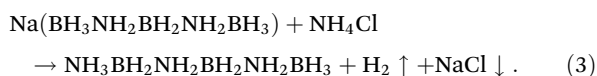
**Fig. 4** Comparison of the $^{11}$B NMR spectra of the main product of the synthesis according to eqn (1) (magenta lines) with the spectra of a product of reaction according to eqn (2) reported by Ewing *et al.*[21] (black lines) both with bottom spectra. Boron spectra show with and without $^1$H decoupling. * indicates $[B(C_6H_5)_4]^-$ anions.



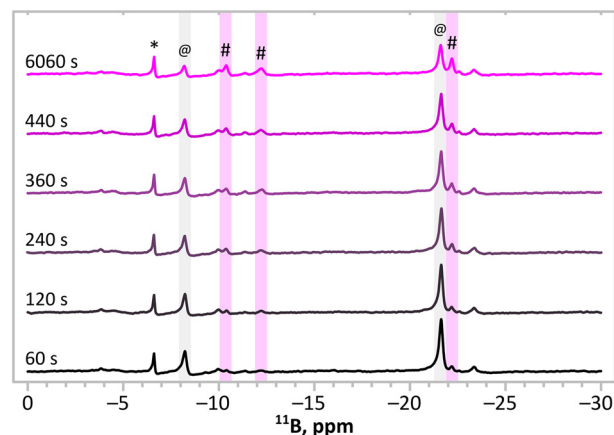**Fig. 5** Sequence of the $^{11}$B{$^1$H} NMR spectra collected *in situ* upon synthesis according to eqn (1). The bottom spectrum shows the mixture of substrates ($t = 60$ s). The top spectrum shows the final mixture of products and substrates ($t = 6060$ s). @ indicates signals from substrates. # indicates signals of the main product. * indicates $[B(C_6H_5)_4]^-$ anions.

(abbreviated as $N_3B_3$) would yield four $BH_2$ triplets from units coordinated by two $NH_2$ groups, three $BH_2$ triplets from units coordinated by $NH_2$ and $NH_3$, and five $BH_3$ quartets of the terminal units altogether. This result would suggest that *ca.* $\frac{3}{4}$ of $(NH_4)(B3N2)$ decomposed to $N_3B_3$ while dissolved in THF.

To get more insights into the processes occurring during the synthesis, we conducted *in situ* $^{11}$B{$^1$H} NMR measurements in THF-$d_8$ to monitor signals of the products and substrates (Fig. 5). The monitoring showed that all three signals from the product(s) (marked with #) arise simultaneously, testifying to the simultaneous progress of reactions described by eqn (1) and (2). Apart from the signals assigned to the substrates and the main product, numerous additional signals which do not change during the reaction are present. These signals come from the moieties that do not play a direct role in the formation of the main product, *e.g.* $[B(C_6H_5)_4]^-$, in which the chemical neighbourhood of the boron atom does not change during the synthesis. The monitored reaction (Fig. 4) was not completed (*i.e.* signals of the substrates were still intense) because of the local depletion of the substrates (no mixing was applied in the NMR test tube inside the spectrometer).

It is worth mentioning that the $^{11}$B NMR spectrum of the main product(s) is very similar to the spectrum reported by Ewing *et al.* in 2013, having the same pattern of three signals: two triplets ($\delta = -10.5$ ppm, $J = 95$ Hz; $\delta = -12.4$ ppm, and $J = 104$ Hz) and a quartet ($\delta = -22.3$ ppm and $J = 95$ Hz)[21] with $4.1 : 3.2 : 5.0$ intensity ratio of the signals (according to our analysis of graphical data shown in that study, Fig. 9a in ref. 19). The report of Ewing *et al.* was focused on the synthesis of a neutral 6-membered chain molecule, B3N3, *via* a direct reaction between Na(B3N2) and ammonium chloride, according to the following equation:[21]

$$Na(BH_3NH_2BH_2NH_2BH_3) + NH_4Cl$$
$$\rightarrow NH_3BH_2NH_2BH_2NH_2BH_3 + H_2 \uparrow + NaCl \downarrow . \quad (3)$$

The reaction, performed in a glyme solution, was accompanied by evolution of hydrogen gas, similarly to our observations.

Ewing *et al.* assumed that the solid product obtained was B3N3, which was based on an NMR study of this material only.[21] The three signals observed were assigned to three boron-containing groups present in the molecule (two $BH_2$ and one $BH_3$). In the case of successful synthesis of B3N3, however, all signals observed should be equally intense ($1 : 1 : 1$), while their intensity ratio was clearly different (Fig. 4). Our analysis suggests that the reaction towards B3N3 is in fact a two-step process (eqn (1) and (2)) and some $(NH_4)(B3N2)$ intermediate (*i.e.* our main target compound) remains in the product. The resulting assignment of NMR signals for both products is given in Table 1.

To further support our claim, we performed more thorough characterisation of the reaction product.

### IR and Raman analysis

Two preeminent sets of bands in the vibrational spectra (IR absorption, Fig. 6; Raman scattering, Fig. 7) of the main product originate from the stretching vibrations of NH (3000–3400 cm$^{-1}$) and BH (2150–2400 cm$^{-1}$) groups. They are

**Table 1** Chemical shifts, *J*-coupling values and assignment of the signals observed in the $^{11}$B NMR spectra of the main product, sample reported by Ewing *et al.*[21] Data for alkali metal M(B3N2) salts[23] given as a reference

| Compound | $-NH_2-BH_2-NH_2-$ | | $NH_3-BH_2-NH_2-$ | | $BH_3-NH_2-$ | |
| --- | --- | --- | --- | --- | --- | --- |
| | $\delta$ [ppm] | $J$ [Hz] | $\delta$ [ppm] | $J$ [Hz] | $\delta$ [ppm] | $J$ [Hz] |
| main product | −10.4 | 101 | −12.3 | 102 | −22.2 | 91 |
| Ewing *et al.*[21] | −10.5 | 95 | −12.4 | 104 | −22.3 | 95 |
| (VBH)(B3N2)[23] | −8.2 | 100 | — | — | −21.6 | 91 |
| Li(B3N2)[23] | −8.4 | 103 | — | — | −22.6 | 90 |
| Na(B3N2)[23] | −8.7 | 99 | — | — | −22.4 | 91 |
| K(B3N2)[23] | −8.6 | 101 | — | — | −22.0 | 89 |
| Rb(B3N2)[23] | −8.4 | 100 | — | — | −21.7 | 90 |
| Cs(B3N2)[23] | −8.4 | 101 | — | — | −21.2 | 94 |

**Fig. 6** Comparison of IR absorption (top in each bracket) and Raman scattering (bottom in each bracket) spectra of the main product of the synthesis according to eqn (1) (magenta) and the spectra of alkali metal M(B3N2) salts. Regions magnified in Fig. 7 (NH stretching and NH bending) are marked with grey fields.



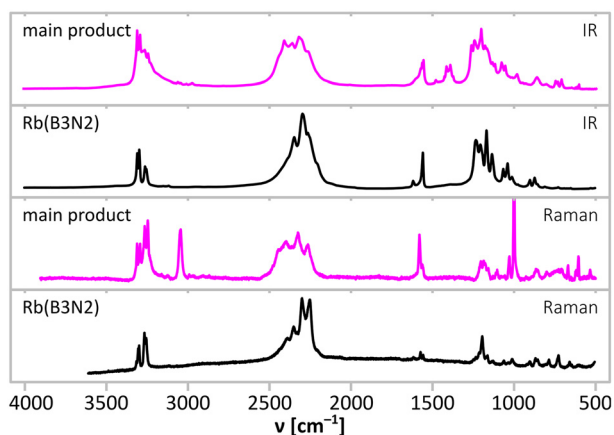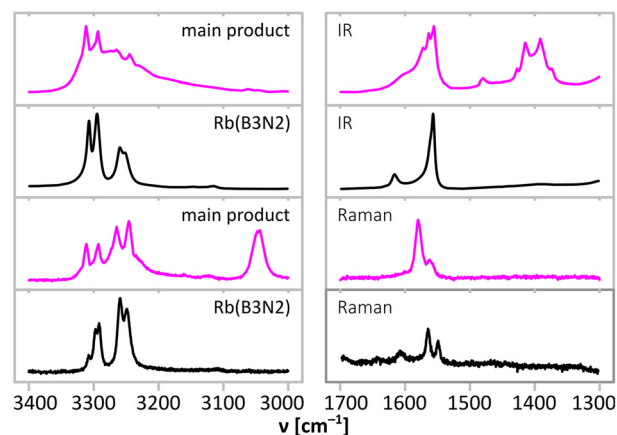**Fig. 7** Comparison of NH stretching (3000–3400 cm$^{-1}$) and NH bending (1300–1700 cm$^{-1}$) regions of IR absorption (top in each bracket) and Raman scattering (bottom in each bracket) spectra of the main product of the synthesis according to eqn (1) (magenta) and alkali metal M(B3N2) salts. Full spectra are presented in Fig. 6.

accompanied by bands coming from the deformation vibrations of NH$_x$ moieties (1400–1600 cm$^{-1}$) as typical of M(B3N2) salts, BH$_x$ deformation modes (below 1350 cm$^{-1}$) and BN stretching (700–800 cm$^{-1}$).

Aside from the bands typical for M(B3N2) salts, the NH stretching region of the Raman spectrum (Fig. 7) contains a relatively low frequency band (peaking at 3041 cm$^{-1}$) originating from ammonium cations. The ammonium cations are known to give a strong Raman band at much lower energies than the [NH$_2$] and [NH$_3$] groups, *e.g.* ammonium chloride gives a single band at 3052 cm$^{-1}$,[32] while ammonium borohydride yields two bands at somewhat higher energies of 3118 cm$^{-1}$ and 3178 cm$^{-1}$.[4,33]

In the higher energy part of NH stretching region, in both IR and Raman spectra, we observe at least 6 distinct bands and a broad band covering the region above 3000 cm$^{-1}$. Four of the bands (3306 cm$^{-1}$, 3288 cm$^{-1}$, 3259 cm$^{-1}$, and 3239 cm$^{-1}$ in IR; 3307 cm$^{-1}$, 3288 cm$^{-1}$, 3260 cm$^{-1}$, and 3240 cm$^{-1}$ in Raman) form a doublet of doublets seen also for heavy alkali metal M(B3N2) salts (Table 2 and Tables S4, S5 in ESI†). It is characteristic for M(B3N2) salts that the higher energy doublet is more intense in the IR spectra, while the lower energy one is stronger in the Raman spectra.[23] The presence of such doublets is caused by Davydov splitting,[34] *i.e.* the interaction of [NH$_2$] groups coexisting within one crystallographic unit cell (resonance of the corresponding oscillators removing their degeneration). A similar split of NH bands was observed in the spectra of Rb(B3N2) and Cs(B3N2), which contain *gauche*-form of (B3N2)$^-$ anions, unlike the lighter analogues featuring straight anions and not showing Davidov split.[23] The split observed here equals ± 9 cm$^{-1}$, which is intermediate between those of ± 4 cm$^{-1}$ and ± 14 cm$^{-1}$ seen for Rb(B3N2) and Cs(B3N2), respectively.[23]

Interestingly, the NH stretching bands of the [NH$_2$] groups of the main product exhibit lower energies than similar bands

in the spectra of alkali metal M(B3N2) salts[21] (Table 2 and Table S4 in ESI†). This very likely results from strong dihydrogen bonds forming a network of interactions between [NH$_x$] and [BH$_x$] moieties of neighbouring (B3N2)$^-$ anions and B3N3 molecules, which stabilise the crystal structure of the main product. A similar effect is observed for two polymorphs of ammonia borane, where orthorhombic LT forms having relatively weak dihydrogen bonds show sharp higher energy bands in the IR spectrum, while tetragonal HT form having relatively strong dihydrogen bonds show broad lower energy bands in the IR spectrum.[35] In general, it is expected that H···H interactions would not only weaken the N–H and B–H bonds but also broaden the absorption bands, which is observed here for the main product.

Two remaining bands observed in the NH stretching region (3224 cm$^{-1}$ and 3268 cm$^{-1}$ in IR) are weaker than the doublets of doublets, and they must originate from the vibrations of terminal [NH$_3$] groups of B3N3. Indeed, they fall in a spectral region typical for terminal [NH$_3$] groups, as observed for ammonia borane (3196 cm$^{-1}$, 3253 cm$^{-1}$ and 3311 cm$^{-1}$). Naturally, it is expected that signals originating from the terminal [NH$_3$] of B3N3 are weaker than those from more numerous [NH$_2$] groups present in both (NH$_4$)(B3N2) and B3N3.

**Table 2** Wavenumbers ([cm$^{-1}$]) of absorption NH stretching bands of [NH$_2$] groups detected in the IR spectrum of the main product at room temperature compared with data for alkali metal M(B3N2) salts: [Li(B3N2), Na(B3N2), K(B3N2), Rb(B3N2), and Cs(B3N2)] at RT.[21]

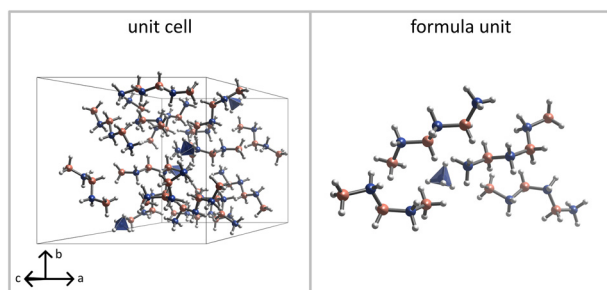| Li(B3N2) | Na(B3N2) | K(B3N2) | Rb(B3N2) | Cs(B3N2) | Main product |
|----------|----------|---------|----------|----------|--------------|
| 3310 s   | 3302 vs  | 3305 vs | 3308 m   | 3313 w   | 3306 vs      |
|          |          |         | 3295 m   | 3287 m   | 3288 vs      |
| 3273 m   | 3256 m   | 3261 m  | 3261 w   | 3261 w   | 3259 m       |
|          |          |         | 3252 w   | 3235 m   | 3239 m       |

**Fig. 8** Visualisation of the unit cell (left) and the asymmetric unit (right) of the crystal structure of the cocrystal comprising one unit of $(NH_4)$ (B3N2) salt and three independent units of B3N3 molecules. Atom code: nitrogen – blue, boron – pink, hydrogen – white.



**Fig. 9** Distribution of H⋯H distances in −N−H⋯H−B− moieties found in CSD database search (accessed by the end of 2022). The distances < 2.8 Å were found for 904 crystal structures. Note the distances: 2.4 Å (double H van der Waals radius)[1] and 1.92 Å present in the structure.

The region of the IR absorption spectrum associated with deformations of the $NH_x$ moieties (Fig. 7) is consistent with these conclusions. One can clearly distinguish signals at *ca.* 1530–1600 cm$^{-1}$, typical for $[NH_2]$ and $[NH_3]$ groups,[23] from the signals at *ca.* 1250–1500 cm$^{-1}$, characteristic for ammonium cations (*cf.* 1402 cm$^{-1}$ for $NH_4Cl$).[36] It is worth to notice that the IR spectra in the 1350–1500 cm$^{-1}$ region show five bands (1374 cm$^{-1}$, 1392 cm$^{-1}$, 1415 cm$^{-1}$, 1427 cm$^{-1}$, and 1479 cm$^{-1}$), and this agrees with the number of deformation modes expected for $NH_4^+$ cations in a low-symmetry environment.

The spectroscopic analysis clearly shows that both $(NH_4)(B3N2)$ and B3N3 moieties constitute the main product, thus confirming the reactions according to eqn (1) and (2).

### Crystal structure of the side product

The chemical composition of the side product of metathesis was confirmed by single-crystal X-ray diffraction measurements (*cf.* ESI†). This compound contains protonated Verkade's base cations and tetraphenylborate anions, $(VBH)[B(C_6H_5)_4]$, proving successful ion exchange in reactions according to eqn (1). The compound crystallises in the $P\bar{1}$ space group with the constituent ions of different polarities, showing no significant interactions, as expected for large ions with a small charge smeared over the entire ion.

### Crystal structure of the main product

As we could not obtain a single crystal of the main product, we were forced to use powder X-ray diffraction (PXRD), supported by DFT calculations and the above-mentioned results of spectroscopic analysis.

Indexing of the PXRD pattern leads to a $P2_1/c$ unit cell with the refined lattice parameters of $a$ = 13.391(10) Å, $b$ = 13.195(8) Å, $c$ = 17.822(12) Å, $\beta$ = 125.86(4)° and $V$ = 2552(3) Å$^3$. Assuming $(NH_4)(B3N2)$ as a product, such unit cell volume would suggest $Z$ = 16 (multiplicity of the general atomic position) and $V/Z$ = 159.5 Å$^3$. However, this $V/Z$ value is too small as the values for K and Rb analogues are larger (167.7 Å$^3$ and 174.3 Å$^3$ respectively),[23] while the size of $NH_4^+$ falls between these two alkali metal cations. Somewhat smaller than the expected $V/Z$ volume suggests that the crystalline phase should contain also the partially dehydrogenated molecules of the product of condensation presented in eqn (2).

To test such scenario, structural models were derived for $(NH_4)(B3N2)$, B3N3 and the $(NH_4)(B3N2)\cdot3(B3N3)$ cocrystal with the components in the 1 : 3 molar ratio as indicated by NMR data. Initial positions of heavy atoms came from simulated annealing using the experimental diffraction data, and refined using Rietveld method. The models were then fully optimised using periodic DFT calculations (Table 3 and ESI†). The theoretical unit cell volume calculated for $(NH_4)(B3N2)$ is significantly larger than those for the models containing B3N3 moieties and the latter are only 4.0–4.5% larger than the experimental value. This degree of overestimation is rather typical for the GGA calculations.

Importantly, the closest H⋯H contacts in the optimised structure of $(NH_4)(B3N2)$ remain unreasonably short (1.40 Å), and outside the distribution observed experimentally for the dihydrogen bonds (usually > 1.80 Å), as shown in Fig. 9. This reconfirms that the main product is not a pure $(NH_4)(B3N2)$. The minimum H⋯H contacts in the optimised crystal structures containing B3N3 are significantly longer (1.60–1.68 Å), and closer to typical values for very strong dihydrogen interactions. Therefore, we have used a theoretical model of the $(NH_4)(B3N2)\cdot3(B3N3)$ cocrystal to refine its crystal structure using the best experimental dataset, Fig. 8 and Fig. S9.3 (ESI).†

**Table 3** Summary of the DFT results. Minimum H⋯H distance is given for fully optimised unit cell: $d(H⋯H)_{min}$ cell opt., and those which lattice vectors were fixed at experimental values: $d(H⋯H)_{min}$ cell fix. The model of $(NH_4)(B3N2)\cdot3(B3N3)$ refined to the experimental XRD data is added for comparison

| Compound | $V$ [Å$^3$] | $\Delta V$ [%] | $d(H⋯H)_{min}$ cell opt. [Å] | $d(H⋯H)_{min}$ cell fix [Å] |
|---|---|---|---|---|
| NH$_4$(B3N2) | 2832.0 | 11.0 | 1.40 | 1.42 |
| (NH$_4$)(B3N2)·3(B3N3) | 2666.1 | 4.5 | 1.60 | 1.62 |
| | 2552.2(30)$^a$ | — | 1.92$^a$ | — |
| B3N3 | 2654.7 | 4.0 | 1.68 | 1.65 |

$^a$ Experimental data with the lower constrain on the H⋯H separation.

The obtained structural model of $(NH_4)(B3N2)\cdot3(B3N3)$ contains four formula units in the unit cell ($Z = 4$) with one asymmetric unit ($Z' = 1$).

The structure is stabilised by strong dihydrogen interactions. Two B3N3 chains adopt *gauche* geometry, and resemble the B3N2 anions in the heavier M(B3N2) salts, M = Rb, Cs.[23] The third B3N3 moiety and (B3N2)$^-$ anion are more straight, closer to the geometry of anionic moieties in the light M(B3N2) salts, M = Li–K.[23,24] The B–N distances of 1.56(2)–1.58(2) Å remain within the range observed in other compounds from this group.

Further improvements of our preliminary experimental structure model, and in particular positions of hydrogen atoms, would require application of neutron diffraction methods, and are beyond the scope of this work.

### Thermal decomposition

The theoretical gravimetric hydrogen content of the 1:3 cocrystals is very large (16.4%). We have studied thermal decomposition of this new compound to assess its hydrogen storage properties. In Fig. 10, we present the results of a simultaneous thermogravimetric and calorimetric analysis of the main product together with gas evolution curves (hydrogen, ammonia, diborane, and borazine) acquired in mass spectrometry experiment of the evolved gases.

The main product is thermally stable below 50 °C. At higher temperatures, one can observe a multistep exothermic decomposition preceded by an endothermic process. During decomposition, a mixture of gases containing borazine, hydrogen, diborane and ammonia is being evolved. Close analysis of TGA/DSC/MS curves suggests that decomposition proceeds in at least 3 steps below 200 °C, but each of them seems to have a similar profile of evolved gases. Interestingly, borazine and hydrogen are the main gaseous products of thermal decomposition, just as in the case of $NH_3BH_3$,[7] but dissimilarly to alkali metal M(B3N2) salts.[23,24] Facile evolution of borazine may be related to the stoichiometry of two components of the main product. $(NH_4)(B3N2)$ and B3N3, both contain 3 boron atoms and 3 nitrogen atoms, just like borazine molecules. Dehydrogenation of $NH_4(B3N2)$ proceeds according to eqn (2), while dehydrogenation of the B3N3 molecule proceeds with formation of a new B–N bond at $[BH_3]$ and $[NH_3]$ terminals according to eqn (4). This reaction was also proposed as the final step of borazine evolution during thermal decomposition of ammonia borane.[37] The formation of pseudo-aromatic borazine is accompanied by dehydrogenation of the elusive head-to-tail cyclohexane-like intermediates, according to eqn (4).

$$NH_3BH_2NH_2BH_2NH_2BH_3 \rightarrow c\text{-}N_3B_3H_{12} + H_2 \rightarrow B_3N_3H_6 + 4H_2 \uparrow \quad (4)$$
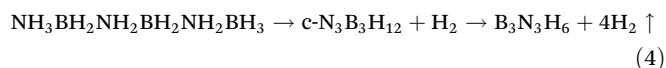
We also observed the formation of $B_2H_6$ and $NH_3$, similarly as in decomposition of Na(B3N2),[23,24] K(B3N2),[23] Rb(B3N2)[23] and Cs(B3N2),[23] which come from fragmentation of (B3N2)$^-$ anions.

As mentioned above, the thermal decomposition of the main product is preceded by an endothermic process. Analogies to
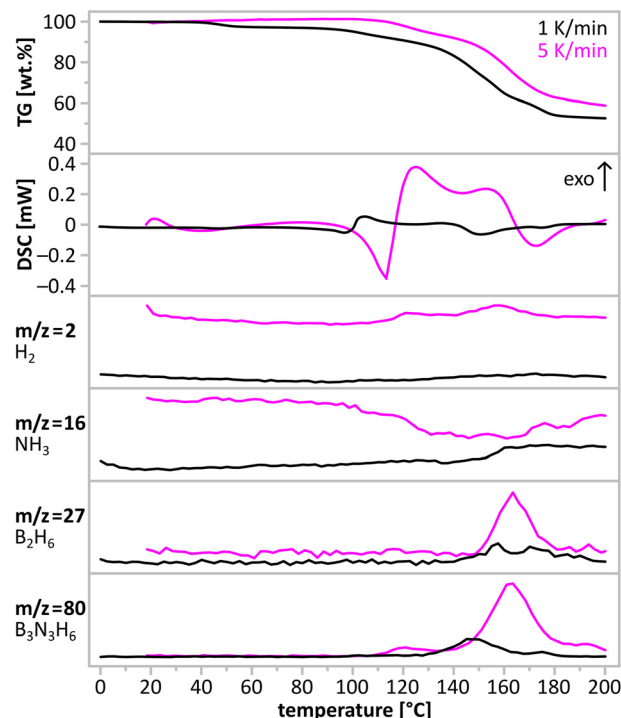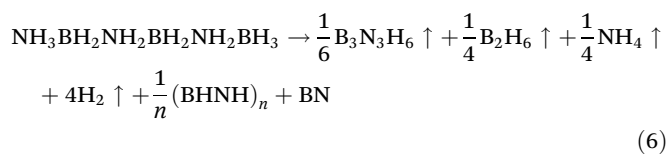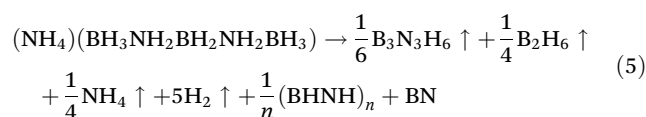


**Fig. 10** Thermogravimetric (TG) and calorimetric (DCS) profiles of the main product set together with MS profiles of the evolved volatile products: $H_2$ (*m/z* = 2), $NH_3$ (*m/z* = 16), $B_2H_6$ (*m/z* = 27), and $B_3N_3H_6$ (*m/z* = 80). The *m/z* values were selected among the strongest, noninterfering signals. Scanning rate: 1 K min$^{-1}$ (black) and 5 K min$^{-1}$ (magenta).

ammonia borane[7] and amidoboranes[12] might suggest melting of the sample. However, direct visual observations ruled out this possibility. Endothermic event is related either to an intermolecular reorganisation or a structural phase transition.

Depending on the heating rate, the decomposition temperature reaches the fastest rate at *ca.* 145 °C and *ca.* 152 °C for 1 K min$^{-1}$ and 5 K min$^{-1}$ scans, respectively. The observed mass loss upon thermal decomposition in the range up to 200 °C, equals *ca.* 45% and surpasses those of alkali metal M(B3N2) salts[23] and parent ammonia borane.[7] Such large observed mass loss may be attributed to the evolution of borazine and other volatiles. The solid residue is amorphous, and consists of boron nitride and polymeric $B_xN_yH_z$ phases as deduced from IR analysis (*cf.* ESI†).

The above-mentioned observations lead to the following overall equations describing thermal decomposition of the two components of the main product:

$$(NH_4)(BH_3NH_2BH_2NH_2BH_3) \rightarrow \frac{1}{6}B_3N_3H_6 \uparrow + \frac{1}{4}B_2H_6 \uparrow$$
$$+ \frac{1}{4}NH_4 \uparrow + 5H_2 \uparrow + \frac{1}{n}(BHNH)_n + BN \quad (5)$$

$$NH_3BH_2NH_2BH_2NH_2BH_3 \rightarrow \frac{1}{6}B_3N_3H_6 \uparrow + \frac{1}{4}B_2H_6 \uparrow + \frac{1}{4}NH_4 \uparrow$$
$$+ 4H_2 \uparrow + \frac{1}{n}(BHNH)_n + BN \quad (6)$$

Theoretical mass losses as explained in eqn (5) and (6) are 43% and 42%, respectively, which reasonably agree with the observed experimental mass loss of *ca.* 45%.

### Theoretical considerations on decomposition pathways

As shown in the previous works, the mechanistic investigation of the decomposition of seemingly simple B–N–H compounds (*e.g.* $NH_3BH_3$ or $MNH_2BH_3$) is a highly demanding task since there are several alternative pathways of their decomposition, which – depending on experiment conditions – may simultaneously affect this process.[38–41] Therefore, we attempted to address in this work only selected aspects influencing thermal decomposition of the examined system, $NH_4(B3N2)$, and of closely related $NH_4BH_4$ and $NH_3BH_3$.

$NH_4(B3N2)$ may be viewed as a derivative of $NH_4BH_4$ where one hydridic hydrogen atom from the borohydride anion is substituted by a $-[NH_2BH_2NH_2BH_3]$ moiety. Such substitution allows for better delocalisation of the anion's negative charge, which should hinder the H···H coupling. This is in good agreement with the differences in thermal stability of these materials, where $NH_4BH_4$ decomposes at *ca.* −40 °C,[31] while decomposition of $NH_4(B3N2)$ can be observed only above +50 °C. $NH_3BH_3$ is the most stable among the considered systems with dehydrogenation onset at +72 °C and rapid decomposition at +112 °C.[8]

The results of our calculations qualitatively reproduce the experimentally observed trend of relative stability of the discussed systems: $NH_4BH_4 < NH_4(B3N2) < NH_3BH_3$ (Table 4). The decomposition of $NH_4BH_4$ in THF requires a small activation barrier of *ca.* 14 kcal $mol^{-1}$, while the reaction barrier for the coupling of $NH_4^+$ cations with $(B3N2)^-$ anions (eqn (2)) in THF is larger, *i.e. ca.* 17 kcal $mol^{-1}$. This translates to *ca.* 100 times slower decomposition of $NH_4(B3N2)$ in comparison to $NH_4BH_4$ under ambient temperature conditions. As known from the literature, dehydrogenation of $NH_3BH_3$ experiences an even higher activation barrier of *ca.* 30 kcal $mol^{-1}$, rendering it stable at room temperature.[39] Thus, $NH_4(B3N2)$ is stabilised with respect to $NH_4BH_4$ and destabilised as compared to $NH_3BH_3$.

The calculations regarding $NH_4(B3N2)$ also explain a rather slow rate of its decomposition towards B3N3, which permits NMR monitoring of this reaction in real time. In this respect, formation of the 3:1 mixture of B3N3 and $NH_4(B3N2)$ could be explained by complexation of $NH_4^+$ cations in the reaction mixture by three bulky B3N3 molecules (formed in the initial stages). Importantly, DFT shows that such complex should be kinetically very stable in the THF solution (*cf.* ESI†). B3N3 molecules partially shield $NH_4^+$ cations making the approach of $(B3N2)^-$ anions more difficult. Additionally, surrounding of the $NH_4^+$ cation by the three large $N_3B_3$ molecules lowers its Lewis acidity, making it thermodynamically less reactive towards $(B3N2)^-$. Indeed, according to our calculations, ligation of $NH_4^+$ with three B3N3 molecules results in an increase in the activation energy of $H_2$ release to 38 kcal $mol^{-1}$, which makes the further decomposition of $NH_4(B3N2)$ towards B3N3 nearly impossible at room temperature. Obviously, such stabilisation is not present in the case of parent $NH_4BH_4$. *cf.* ESI† for further details of the calculated reaction paths.

Noteworthy, our estimation of reaction barrier (in THF) for cyclisation of B3N3 or intramolecular $H_2$ evolution from $NH_3BH_3$ gives values higher than decomposition of the $NH_4^+$ complex with B3N3 (Table 4), which is in agreement with experimental findings that these systems are stable.

## Conclusions

Synthesis of hydrogen-rich $(NH_4)(B3N2)$ salts was attempted *via* a metathetical approach using precursors which contained weakly coordinating ions. The obtained product, however, corresponds to a mixture of ionic $(NH_4)(B3N2)$ and neutral B3N3 forming cocrystals in a molar ratio of 1:3. Based on available $^{11}B$ NMR data, the main product was found to be very similar to the samples reported earlier by Ewing *et al.*[21] as B3N3. The B3N3 moiety forms due to partial decomposition of $(NH_4)(B3N2)$ occurring *in situ* during the synthesis.

Despite its high hydrogen content of 16.4%, the new compound cannot act 'as prepared' as a self-standing solid-state hydrogen reservoir as it decomposes *via* a set of exothermic events while evolving a mixture of volatile gaseous products such as borazine, diborane and ammonia, aside from hydrogen. Thus, the spontaneous, gradual decomposition cannot easily be avoided *via* pressurisation, and deeper chemical modifications, like formation of mixed-cation salts, would be required to stabilise such compounds. However, it is possible that templating our product in porous matrixes could result in a substantial improvement in the purity of the evolved hydrogen, similarly as it was observed for ammonia borane.[42]

## Experimental

### Reagents

All operations were performed in an inert Ar atmosphere inside gloveboxes, MBRAUN Labmaster DP or Vigor SG1200 ($O_2$, $H_2O$ < 1.0 ppm). Commercially available reagents and solvents were used: $NH_3BH_3$ (98%, JSC Aviabor), $NH_4B(C_6H_5)_4$ (99%, Sigma-Aldrich (later denoted as SA), $C_4H_8O$ (99%, SA), and $CH_2Cl_2$ (99%, SA). The synthesis of $(C_{18}H_{39}N_4PH)$ $(BH_3NH_2BH_2NH_2BH_3)$ was performed according to the route

**Table 4** Summary of the results of DFT calculations for decomposition processes of selected systems *via* H−H coupling in THF solution

| Dehydrogenation process | $E_a$ [kcal $mol^{-1}$] |
|---|---|
| $(NH_4)^+(BH_4)^- \rightarrow NH_3BH_3 + H_2\uparrow$ | 14 |
| $(NH_4)^+(B3N2)^- \rightarrow B3N3 + H_2\uparrow$ | 17 |
| $3B3N3\cdot(NH_4)^+(B3N2)^- \rightarrow 4B3N3 + H_2\uparrow$ | 38 |
| $B3N3 \rightarrow c\text{-}N_3B_3H_{12} + H_2\uparrow$ | 42 |
| $2NH_3BH_3 \rightarrow NH_3BH_2NH_2BH_3 + H_2\uparrow$ | 56 |

described in our earlier paper.[23] For NMR measurements, we used THF-d8 (99.5 atom% D, SA).

## Infrared absorption spectroscopy

IR spectra were measured in the standard range of 400–4000 $cm^{-1}$ using a Fourier Transform IR spectrometer Vertex 80v from Bruker. Samples were examined using KBr pellets prepared using anhydrous KBr (99%, SA) additionally dried at 150 °C for 24 h.

## Raman spectroscopy

Raman scattering measurements were done using a Raman microscopy setup from Jobin Yvon T64000 with a Si CCD detector and a Kr–Ar gas laser from Spectraphysics. We used green 514.5 nm excitation line. For the measurements, small doses of samples were placed in 0.5 mm-thick quartz capillaries sealed in an inert gas atmosphere.

## Nuclear magnetic resonance

$^{1}B$ NMR spectra with and without $^{1}H$ decoupling were recorded using an Agilent 700 MHz spectrometer with a Direct Drive 2 console and a 5 mm room temperature broadband probe. We used deuterated tetrahydrofuran ($d_8$-THF) as a solvent. The number of scans has been set to 256, the interscan delay to 1 s and the acquisition time to 200 ms. The spectra were acquired at 25 °C. The exponential apodisation has been used during processing (line broadening of 5 Hz).

## Thermogravimetric analysis

Thermal decomposition was investigated using a STA 410 thermal analyser from Netzsch, in the temperature range from −10 °C to +200 °C. A STA 449 allows for simultaneous thermogravimetric analysis, differential scanning calorimetry and evolved gas analysis by means of mass spectrometry. The samples were loaded into alumina crucibles inside a glovebox. Helium was used as a carrier gas. Evolved gases were analysed using a QMS 403C Aëolos MS from Pfeiffer–Vacuum. The transfer line was preheated to 100 °C to avoid condensation of residues.

## Powder X-ray diffraction

PXRD measurements were conducted on samples sealed in 0.5 mm thick quartz capillaries in an inert atmosphere. Two diffractometers were used: a Panalytical X'Pert Pro with a linear PIXcel Medipix2 detector (parallel beam; the $CoK\alpha_{12}$ radiation) and a Bruker D8 Discover with a 2D Vantec detector (parallel beam; the $CuK\alpha_{12}$ radiation).

## Crystal structure solution of the main product

Diffraction signals were indexed using a X-cell[43] and the initial structural model was obtained using the FOX software,[44] while the Rietveld refinement has been performed using a Jana2006.[45] Pseudovoigt functions with the Berar–Baldinozzi asymmetry were used for the modelling of diffraction profiles. The restraints were used during refinement for the N–H and B–H distances (at 0.900(10) Å and 1.100(10) Å, respectively,

Fig. S9. 2†), and the angles related to hydrogen atoms (to 109.47° with tolerance of ca. 0.5°). The N–B distances were set to the value 1.57(1) Å. The atomic displacement parameters of B and N atoms were set equal, while those of H atoms were constrained according to the riding model. The bottom constraint of 1.91 Å for H⋯H distances was applied for the final refinement. Further details on the crystal structure may be obtained from CCDC/FIZ Karlsruhe on quoting the CSD deposition no. 2193624.

## Crystal structure solution of the side product

The crystal of the compound was covered with perfluorinated oil (Krytox 1531). Data collection and reduction were performed using an Agilent Supernova X-ray diffractometer with Kα-Cu radiation (microsource), data reduction being performed using the CrysAlisPro software (v. 40.99).[46] Structure solution: SHELXT,[47] refinement against $F^2$ in Shelxl-2018, with ShelXle as GUI software.[48] The disorder of the $-OC(CF_3)_3$ groups was resolved using DSR.[49] Further details on the crystal structure may be obtained from CCDC/FIZ Karlsruhe on quoting the CSD deposition no. 2195203.

## Density functional theory

DFT calculations for the solid state were performed using the CASTEP.[50] The initial structural models were derived from the experimental data, as described above. Generalised gradient approximation (GGA) was used with the PBE functional and Tkatchenko–Scheffler dispersive correction.[51] A cutoff value of 500 eV was applied to achieve good energy convergence. The density of the $k$-point grid was set below 0.1 $Å^{-1}$ and ultrasoft generated on the fly pseudopotentials was used as they provide more accurate lattice parameters.

The molecular DFT calculations were performed using the Orca 5.0.3 package[52] by the $r^2$SCAN-3c method used for structure optimisations and thermochemistry calculations. THF solvation was simulated using the CPCM model. Reaction barriers were determined using the nudged elastic bond method (NEB) with transition state optimised with $r^2$SCAN-3c.[53] To achieve a better accuracy, single-point energies for the optimised structures were calculated with ωB97X-V functional[54] with def2-TZVP basis set,[55] def2/J auxiliary basis set[56] and D4 dispersion correction.[57]

## Graphical presentation

Visualisations of crystal structures were performed with Vesta.[58] Illustrations have been prepared using Inkscape 0.92.1.[59]

# Conflicts of interest

There are no conflicts of interests to declare.

## Acknowledgements

## References

1 T. Richardson, S. de Gala, R. H. Crabtree and P. E. M. Siegbahn, *J. Am. Chem. Soc.*, 1995, **117**, 12875–12876.

2 W. T. Klooster, T. F. Koetzle, P. E. M. Siegbahn, T. B. Richardson and R. H. Crabtree, *J. Am. Chem. Soc.*, 1999, **121**, 6337–6343.

3 E. Magos-Palasyuk, T. Palasyuk, P. Zaleski-Ejgierd and K. Fijalkowski, *CrystEngComm*, 2014, **16**, 10367–10370.

4 S. Filippov, J. B. Grinderslev, M. S. Andersson, J. Armstrong, M. Karlsson, T. R. Jensen, J. Klarbring, S. I. Simak and U. Häussermann, *J. Phys. Chem. C*, 2019, **123**, 28631–28639.

5 S. G. Shore and R. W. Parry, *J. Am. Chem. Soc.*, 1955, **77**, 6084–6085.

6 U. B. Demirci, *Energies*, 2020, **13**, 3071.

7 F. Baitalow, J. Baumann, G. Wolf, K. Jaenicke-Rößler and G. Leitner, *Thermochim. Acta*, 2002, **391**, 159–168.

8 J. Baumann, F. Baitalow and G. Wolf, *Thermochim. Acta*, 2005, **430**, 9–14.

9 A. Al-Kukhun, H. T. Hwang and A. Varma, *Int. J. Hydrogen Energy*, 2013, **38**, 169–179.

10 DOE Technical Targets for Onboard Hydrogen Storage for Light-Duty Vehicles.

11 Y. S. Chua, P. Chen, G. Wu and Z. Xiong, *Chem. Commun.*, 2011, **47**, 5116.

12 R. Owarzany, P. Leszczyński, K. Fijalkowski and W. Grochala, *Crystals*, 2016, **6**, 88.

13 H. V. K. Diyabalanage, T. Nakagawa, R. P. Shrestha, T. A. Semelsberger, B. L. Davis, B. L. Scott, A. K. Burrell, W. I. F. David, K. R. Ryan, M. O. Jones and P. P. Edwards, *J. Am. Chem. Soc.*, 2010, **132**, 11836–11837.

14 I. V. Kazakov, A. V. Butlak, P. A. Shelyganov, V. V. Suslonov and A. Y. Timoshkin, *Polyhedron*, 2017, **127**, 186–190.

15 R. Owarzany, T. Jaroń, P. J. Leszczyński, K. J. Fijalkowski and W. Grochala, *Dalton Trans.*, 2017, **46**, 16315–16320.

16 J. Luo, X. Kang and P. Wang, *Energy Environ. Sci.*, 2013, **6**, 1018–1025.

17 N. A. Shcherbina, I. V. Kazakov and A. Y. Timoshkin, *Russ. J. Gen. Chem.*, 2017, **87**, 2875–2877.

18 M. F. Hawthorne, S. S. Jalisatgi, A. V. Safronov, H. B. Lee and J. Wu, *Chemical Hydrogen Storage Using Polyhedral Borane Anions and Aluminum-Ammonia-Borane Complexes*, 2010.

19 G. Xia, Y. Tan, X. Chen, Z. Guo, H. Liu and X. Yu, *J. Mater. Chem. A*, 2013, **1**, 1810–1820.

20 N. Biliškov, A. Borgschulte, K. Užarević, I. Halasz, S. Lukin, S. Milošević, I. Milanović and J. G. Novaković, *Chem. – Eur. J.*, 2017, **23**, 16274–16282.

21 W. C. Ewing, P. J. Carroll and L. G. Sneddon, *Inorg. Chem.*, 2013, **52**, 10690–10697.

22 W. C. Ewing, A. Marchione, D. W. Himmelberger, P. J. Carroll and L. G. Sneddon, *J. Am. Chem. Soc.*, 2011, **133**, 17093–17099.

23 R. Owarzany, K. J. Fijalkowski, T. Jaroń, P. J. Leszczyński, Ł. Dobrzycki, M. K. Cyrański and W. Grochala, *Inorg. Chem.*, 2016, **55**, 37–45.

24 K. J. Fijalkowski, T. Jaroń, P. J. Leszczyński, E. Magos-Palasyuk, T. Palasyuk, M. K. Cyrański and W. Grochala, *Phys. Chem. Chem. Phys.*, 2014, **16**, 23340–23346.

25 X. Chen, X. Jiang, Y. Jing and X. Chen, *Chem.– Asian J.*, 2021, **16**, 2475–2480.

26 I. C. Evans, Dissertation, University of Birmingham, 2011.

27 K. R. Ryan, Dissertation, University of Oxford, 2011.

28 A. Starobrat, M. J. Tyszkiewicz, W. Wegner, D. Pancerz, P. A. Orłowski, P. J. Leszczyński, K. J. Fijalkowski, T. Jaroń and W. Grochala, *Dalton Trans.*, 2015, **44**, 19469–19477.

29 T. Jaroń, W. Wegner, K. J. Fijałkowski, P. J. Leszczyński and W. Grochala, *Chem. – Eur. J.*, 2015, **21**, 5689–5692.

30 T. Jaroń, P. A. Orłowski, W. Wegner, K. J. Fijałkowski, P. J. Leszczyński and W. Grochala, *Angew. Chem., Int. Ed.*, 2015, **54**, 1236–1239.

31 R. W. Parry, D. R. Schultz and P. R. Girardot, *J. Am. Chem. Soc.*, 1958, **80**, 1–3.

32 R. S. Krishnan, *Proc. Ind. Acad. Sci., A*, 1947, **26**, 432.

33 A. Karkamkar, S. M. Kathmann, G. K. Schenter, D. J. Heldebrant, N. Hess, M. Gutowski and T. Autrey, *Chem. Mater.*, 2009, **21**, 4356–4358.

34 A. S. Davydov, *Theory of Molecular Excitons*, Springer, 1971.

35 A. Paolone, F. Teocoli, S. Sanna, O. Palumbo and T. Autrey, *J. Phys. Chem. C*, 2013, **117**, 729–734.

36 W. E. Wallace, in *NIST Standard Reference Database Number 69*, ed. P. Linstrom and W. Mallard, National Institute of Standards and Technology, 2018.

37 H. Wu, W. Zhou and T. Yildirim, *J. Am. Chem. Soc.*, 2008, **130**, 14834–14839.

38 M. T. Nguyen, V. S. Nguyen, M. H. Matus, G. Gopakumar and D. A. Dixon, *J. Phys. Chem. A*, 2007, **111**, 679–690.

39 P. M. Zimmerman, Z. Zhang and C. B. Musgrave, *J. Phys. Chem. Lett.*, 2011, **2**, 276–281.

40 C. W. Hamilton, R. T. Baker, A. Staubitz and I. Manners, *Chem. Soc. Rev.*, 2009, **38**, 279–293.

41 J. Li, S. M. Kathmann, H.-S. Hu, G. K. Schenter, T. Autrey and M. Gutowski, *Inorg. Chem.*, 2010, **49**, 7710–7720.

42 A. Gutowska, L. Li, Y. Shin, C. M. Wang, X. S. Li, J. C. Linehan, R. S. Smith, B. D. Kay, B. Schmid, W. Shaw, M. Gutowski and T. Autrey, *Angew. Chem., Int. Ed.*, 2005, **44**, 3578–3582.

43 M. A. Neumann, *J. Appl. Crystallogr.*, 2003, **36**, 356–365.

44 V. Favre-Nicolin and R. Černý, *J. Appl. Crystallogr.*, 2002, **35**, 734–743.

45 V. Petříček, M. Dušek and L. Palatinus, *Z. Kristallogr. - Cryst. Mater.*, 2014, **229**, 345–352.

46 Agilent, 2014.

47 G. M. Sheldrick, *Acta Crystallogr., Sect. A: Found. Adv.*, 2015, **71**, 3–8.

48 C. B. Hübschle, G. M. Sheldrick and B. Dittrich, *J. Appl. Crystallogr.*, 2011, **44**, 1281–1284.

49 D. Kratzert, J. J. Holstein and I. Krossing, *J. Appl. Crystallogr.*, 2015, **48**, 933–938.

50 S. J. Clark, M. D. Segall, C. J. Pickard, P. J. Hasnip, M. I. J. J. Probert, K. Refson and M. C. Payne, *Z. Kristallogr.*, 2005, **220**, 567–570.

51 A. Tkatchenko and M. Scheffler, *Phys. Rev. Lett.*, 2009, **102**, 073005.

52 F. Neese, F. Wennmohs, U. Becker and C. Riplinger, *J. Chem. Phys.*, 2020, **152**, 224108.

53 S. Grimme, A. Hansen, S. Ehlert and J.-M. Mewes, *J. Chem. Phys.*, 2021, **154**, 064103.

54 N. Mardirossian and M. Head-Gordon, *Phys. Chem. Chem. Phys.*, 2014, **16**, 9904.

55 F. Weigend and R. Ahlrichs, *Phys. Chem. Chem. Phys.*, 2005, **7**, 3297.

56 F. Weigend, *Phys. Chem. Chem. Phys.*, 2006, **8**, 1057.

57 E. Caldeweyher, S. Ehlert, A. Hansen, H. Neugebauer, S. Spicher, C. Bannwarth and S. Grimme, *J. Chem. Phys.*, 2019, **150**, 154122.

58 K. Momma and F. Izumi, *J. Appl. Crystallogr.*, 2011, **44**, 1272–1276.

59 Inkscape project, 2017.